Thermoelectric properties of epitaxial ScN films deposited by reactive magnetron sputtering onto MgO(001) substrates

Polina V. Burmistrova, Jesse Maassen, Tela Favaloro, Bivas Saha, Shuaib Salamat, Yee Rui Koh, Mark S. Lundstrom, Ali Shakouri, and Timothy D. Sands

Citation: Journal of Applied Physics **113**, 153704 (2013); doi: 10.1063/1.4801886
View online: http://dx.doi.org/10.1063/1.4801886
View Table of Contents: http://scitation.aip.org/content/aip/journal/jap/113/15?ver=pdfcov
Published by the AIP Publishing

Thermoelectric properties of epitaxial ScN films deposited by reactive magnetron sputtering onto MgO(001) substrates

Polina V. Burmistrova,[1,2] Jesse Maassen,[1] Tela Favaloro,[3] Bivas Saha,[2,4] Shuaib Salamat,[1] Yee Rui Koh,[1,2] Mark S. Lundstrom,[1,2] Ali Shakouri,[1,2,3] and Timothy D. Sands[1,2,4]
[1]*School of Electrical and Computer Engineering, Purdue University, West Lafayette, Indiana 47907, USA*
[2]*Birck Nanotechnology Center, Purdue University, West Lafayette, Indiana 47907, USA*
[3]*School of Engineering, University of California Santa Cruz, Santa Cruz, California 95064, USA*
[4]*School of Materials Engineering, Purdue University, West Lafayette, Indiana 47907, USA*

(Received 14 January 2013; accepted 1 April 2013; published online 16 April 2013)

Epitaxial ScN(001) thin films were grown on MgO(001) substrates by dc reactive magnetron sputtering. The deposition was performed in an Ar/N_2 atmosphere at 2×10^{-3} Torr at a substrate temperature of 850 °C in a high vacuum chamber with a base pressure of 10^{-8} Torr. In spite of oxygen contamination of 1.6 ± 1 at. %, the electrical resistivity, electron mobility, and carrier concentration obtained from a typical film grown under these conditions by room temperature Hall measurements are 0.22 mΩ cm, 106 $cm^2 V^{-1} s^{-1}$, and 2.5×10^{20} cm^{-3}, respectively. These films exhibit remarkable thermoelectric power factors of 3.3–3.5 $\times 10^{-3}$ W/mK^2 in the temperature range of 600 K to 840 K. The cross-plane thermal conductivity is 8.3 W/mK at 800 K yielding an estimated ZT of 0.3. Theoretical modeling of the thermoelectric properties of ScN calculated using a mean-free-path of 23 nm at 300 K is in very good agreement with the experiment. These results also demonstrate that further optimization of the power factor of ScN is possible. First-principles density functional theory combined with the site occupancy disorder technique was used to investigate the effect of oxygen contamination on the electronic structure and thermoelectric properties of ScN. The computational results suggest that oxygen atoms in ScN mix uniformly on the N site forming a homogeneous solid solution alloy. Behaving as an n-type donor, oxygen causes a shift of the Fermi level in ScN into the conduction band without altering the band structure and the density of states.
 [http://dx.doi.org/10.1063/1.4801886]

I. INTRODUCTION

Scandium nitride (ScN), a semiconducting transition metal nitride, has remarkable physical properties such as high chemical stability, melting point (about 2600 °C), and mechanical hardness.[1,2] ScN adopts a rocksalt (B1) crystal structure with a lattice parameter of 4.50–4.52 Å.[3,4] The most common ScN thin-film deposition techniques are molecular beam epitaxy (MBE),[5–8] reactive magnetron sputtering,[2–4,9–14] and hydride vapor phase epitaxy (HVPE).[15,16]

Theoretical and experimental studies have shown that ScN is an n-type semiconductor with an indirect bandgap of about 0.9 eV.[17] The value of the direct bandgap at the gamma point has been reported to be in the range of 2.1–2.6 eV.[10] The electron concentration is typically in the degenerate range of 10^{20}–10^{22} cm^{-3} (Refs. 11, 12, 14, and 15) values that were originally attributed to a high level (up to 20%) of nitrogen vacancies.[18] Since Sc has one of the highest affinities for oxygen among transition metals,[10] oxygen, which acts as a donor, is a common impurity that enhances the conductivity of ScN films.[10,15] The oxygen incorporation most likely occurs during deposition[10] rather than as a result of grain boundary diffusion during postgrowth exposure to oxygen.[13] The electron mobility of sputtered ScN thin films is typically in the 30–100 $cm^2 V^{-1} s^{-1}$ range. The highest reported electron mobility, 176 $cm^2 V^{-1} s^{-1}$, was measured for a film grown by HVPE.[15] This previous study also demonstrated that post-growth annealing at 1000 °C in a Mg atmosphere leads to a slight reduction of carrier concentration, from 2.3 to 1.1 $\times 10^{20}$ cm^{-3}, and a significant increase in Hall mobility, from 19 to 158 $cm^2 V^{-1} s^{-1}$.[15] In this work, halogen or hydrogen was proposed to be the principal donor during the growth and were presumed to be responsible for the degenerate carrier concentration in the ScN thin films.[15] However, no chemical analysis was attempted in order to prove this assertion.

Recently, ScN is receiving increased attention for its versatility in emerging applications[14,19–23] including optoelectronics[19,20] and thermoelectrics.[14,21–23] In GaN-based optoelectronics, ScN interlayers have proven to be efficient in reducing dislocation densities.[19] ScN can also be used as a substrate or contact material[20] since the (111) plane of ScN is lattice-matched to the (0001) plane of GaN. In the case of thermoelectrics, ScN is being explored as the semiconductor layer in metal/semiconductor superlattices for high-temperature thermionic energy conversion[21–23] and as a high-temperature thermoelectric material on its own accord.[14] With regards to ScN as a stand-alone thermoelectric material, an electron mobility of 30 $cm^2 V^{-1} s^{-1}$ and electron concentration of 1×10^{21} cm^{-3} has been reported on ScN(111) epitaxial films deposited on a (0001) sapphire substrate. A Seebeck coefficient of −86 μV/K at 800 K resulted in a power factor of 2.5×10^{-3} W/mK^2.[2,14]

For the present study, high quality epitaxial ScN(001) films were grown on MgO(001) substrates by dc reactive magnetron sputtering. The thermoelectric properties of ScN thin films were assessed by a combination of experimental

and theoretical techniques. Despite the oxygen contamination, the films show exceptional electronic and thermoelectric properties. Modeling of the thermoelectric properties is found to yield results that are in good agreement with experimental results. The effect of oxygen content on the electronic structure and properties of ScN was evaluated using first-principles density functional theory (DFT) calculations combined with the site occupancy disorder (SOD) technique.

II. EXPERIMENTAL PROCEDURES

ScN thin films with thicknesses in the range of 480-520 nm were deposited by dc reactive magnetron sputtering in a high vacuum chamber with a base pressure of 10^{-8} Torr (PVD Products, Inc.,) on 1×1 cm MgO(001) and Si(001) substrates. The Si substrate was mainly used for temperature calibration. Prior to the deposition, the substrates were ultrasonically cleaned in toluene, acetone, and methanol and blown dry in nitrogen. The deposition was carried out in an Ar(10 sccm)/N_2(3 sccm) atmosphere at 2×10^{-3} Torr. The 99.99% pure 2 in. Sc target was sputtered at 150 W in a dc constant power mode. The substrate temperature was maintained at 830 ± 20 °C using a SiC heater and controlled by a thermocouple and an infrared pyrometer. The first pyrometer temperature measurement was taken from a pure Si 1×1 cm substrate since the MgO substrate is optically transparent in the pyrometer wavelength range. Another temperature measurement was taken from both Si and MgO substrates after about 100 nm of a ScN thin film was deposited. The samples were cooled at a rate of 20 °C per minute.

The microstructures and orientations of the resultant films were characterized by x-ray diffraction (XRD) and transmission electron microscopy (TEM) using CuK_α radiation in a Panalytical X'pert diffractometer and an FEI Titan 80-300 transmission electron microscope, respectively. Cross-sectional samples for TEM study were prepared by the focused ion beam (FIB) *in-situ* lift-out technique using an FEI Nova 200 dual beam scanning electron microscopy (SEM)/FIB equipped with a Klöcke nanomanipulator. Plan-view samples were obtained by a mechanical grinding and polishing followed by ion milling to electron transparency using a 5 kV Ar^+-ion beam at a 8° incident angle in a Gatan PIPS system. Surface morphology was examined by SEM using the same FEI Nova 200 dual beam SEM/FIB. The elemental composition of the ScN films was obtained by Rutherford Backscattering Spectroscopy (RBS) using nuclear reaction analysis (NRA), a technique that provides improved sensitivity and accuracy for oxygen. The analysis was conducted by Evans Analytical Group (EAG).

Hall measurements were carried out using an MMR Technologies system. An H 50 Van der Pauw controller was used in order to perform the resistivity measurements prior to obtaining the Hall mobility and electron concentrations. Indium was used as a contact material.

The thermoelectric properties of the ScN film were obtained inside a thermostat under $\sim 10^{-6}$ Torr vacuum in the 300-840 K temperature range, measured in 50 K intervals. The sample was mounted in a floating configuration across a measurement stage. The electrical conductivity in the conventional Van der Pauw configuration and the Seebeck coefficient were measured simultaneously to ensure that each value was obtained under identical conditions. A total of eight resistance measurements were taken at each temperature, including both polarities. Several temperature gradients were established at each of the different ambient temperatures, such that the Seebeck coefficient was determined as the linear relationship between the induced voltages and the temperature differences. Sufficient time was allowed to establish thermal equilibrium before recording the voltage. Using known types of thermocouple calibrations over the temperature range, the absolute Seebeck voltage of the sample was extracted from the total measured voltage.

The time-domain thermoreflectance (TDTR) technique was employed to measure the thermal conductivity of the ScN thin films.[24–26] In the TDTR setup, a Ti:sappire laser was used to create femtosecond laser pulses with ~12.5 ns repetition rate and a fixed laser power of 25 MW. The laser pulses were split into a pump beam (18 MW) and a probe beam (7 MW). The pump beam, which induced localized heating of the sample, was modulated with an electro-optic modulator (EOM) at a modulation frequency of 835 kHz. A Si-photodetector and an RF lock-in amplifier were used to capture the reflected probe beam signal. The sample was coated with a 70 nm aluminum film to absorb the incident laser light, acting as a transducer. The thermal conductivity of the ScN thin film was obtained by fitting the measurement data with a 3D thermal model based on thermal quadrupoles.[26]

Plane-wave self-consistent field (PWSCF) implementation of DFT was employed with a generalized gradient approximation (GGA) to the exchange correlation energy[27] and ultrasoft pseudopotentials[28] to represent the interaction between ionic cores and valence electrons. Plane-wave basis sets (PWs) with cut-off energies of 30 Ry and 180 Ry were used to represent the electronic wave functions and charge densities, respectively. Integration over the Brillouin zone was carried out using a gamma-centered grid with a $5 \times 5 \times 5$ mesh of k-points for all calculations having 222 supercells. Hubbard U-corrections with $U = 3.5$ eV were used for the Sc atoms to accurately describe the electronic structure of ScN.[17,29]

The SOD technique[30] was used to obtain the symmetry inequivalent configurations (SIC) of a 222 ScN supercell. To investigate the effect of oxygen on ScN's electronic properties, extensive simulations with a 222 ScN supercell having oxygen concentrations of 1.56, 3.12, 4.68, and 6.25 at. %, respectively, were performed. For all calculations, structures were relaxed until forces on each atom were less than 0.001 Ry/Bohr.

The thermoelectric transport parameters, electrical conductivity, and Seebeck coefficient were calculated using[31]

$$\sigma = q^2 \int_{-\infty}^{+\infty} dE \left[-\frac{\partial f}{\partial E} \right] \Sigma(E), \tag{1}$$

$$S = \frac{q}{\sigma T} \int_{-\infty}^{+\infty} dE \left[-\frac{\partial f}{\partial E} \right] \Sigma(E)(E - E_F), \tag{2}$$

where q is the electron charge, T is the temperature, f is the Fermi-Dirac distribution function, E_F is the Fermi level, and $\Sigma(E)$ is the so-called transport distribution.[31] The transport distribution is commonly expressed in terms of the band velocity along the transport direction and the scattering time. However, an equivalent formulation based on the Landauer approach can also be used, and is generally simpler from a computational perspective. With the Landauer approach, the transport distribution is obtained with the following expression:[32]

$$\Sigma(E) = \frac{L^2}{h} M(E) T(E), \tag{3}$$

where $M(E)$ is the number of conducting channels at the energy E, L is the length of the conductor, $T(E) = \lambda(\mathrm{E})/(\lambda(\mathrm{E}) + \mathrm{L})$ is the transmission coefficient corresponding to the probability of an electron traveling from one side ($\mathrm{z} = 0$) of the sample to the other ($\mathrm{z} = \mathrm{L}$), and λ is the mean-free-path (MFP) for backscattering representing the average distance traveled along the transport direction before a forward moving electron becomes backward moving. Note that the Landauer formulation is valid in ballistic, quasi-ballistic, and diffusive transport regimes. In the case of diffusive transport ($\mathrm{L} \gg \lambda$), $T(E)$ is written as λ/L. This approach can be shown to be equivalent to the standard transport distribution.[32]

As is evident from these expressions, in order to calculate the transport properties one needs to know two basic parameters: the distribution of modes $M(E)$ and the mean-free-path λ. The distribution of modes depends on the electronic dispersion of ScN,[32] which was calculated in the entire Brillouin zone with DFT, using the generalized gradient approximation, a cut-off energy of 700 eV for the plane-wave basis, a k-point mesh of $55 \times 55 \times 55$ (with unit cell) and the experimental lattice constant of 4.52 Å. The experimental band gap of 0.9 eV was set by rigidly shifting the energy of the valence and conduction bands. For the MFP, a simple expression valid for the case of acoustic phonon scattering was assumed.

III. RESULTS AND DISCUSSION

The 2θ-ω diffraction pattern of a ScN thin film deposited on an MgO(001) substrate is shown in Fig. 1. The pattern indicates that the ScN film is $\langle 002 \rangle$ oriented. No other reflections were observed. The 002 peak position is 40.01°, corresponding to a lattice constant of 4.50 Å in the growth direction, a value that is closely matched to the reported relaxed ScN lattice constant.[4] The insert in Fig. 1 is a rocking curve of the 002 ScN reflection with a full-width-at-half-maximum (FWHM) of 0.675°. The reciprocal space map (RSM) obtained for the 024 ScN reflection (not shown) indicates epitaxial growth of a fully relaxed ScN film on the MgO substrate with a mosaic spread of 0.086°.

Figure 2 is an FESEM plan-view image of a ScN film obtained using a high resolution through-lens backscattering electron detector. The square densely packed features with an average feature size of 40 nm are present on the film surface. These features correspond to the formation of

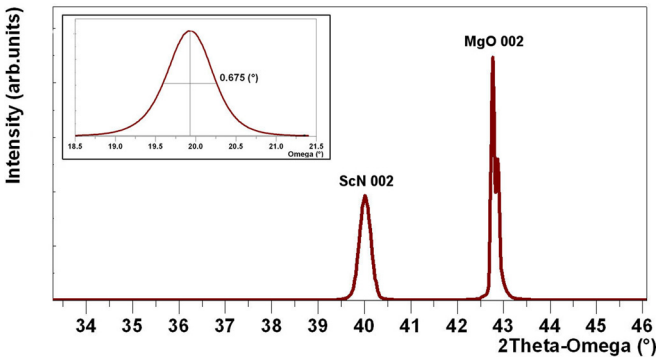

FIG. 1. 2θ-ω diffraction pattern from ScN thin film sputtered onto MgO(001) substrate. A rocking curve (insert) of 002 ScN reflection reveals a FWHM of 0.675°.

kinetically driven mound structures. Similar formations were previously observed in some semiconductors and transmission metal nitrides as well as in ScN single crystalline sputtered thin films.[4,9] As described in Ref. 4, an Ehrlich-Schwoebel surface diffusion barrier inhibits adatom migration down steps, thereby promoting nucleation on terraces and leading to the formation of mounds. As the film growth continues, mounds connect along the edges with the development of the cusps. Shadowing during further deposition and reduced adatom mobility at cusps leads to nanopipe formation along the mound edges and surface roughening. Thus, these features with four-fold symmetry, as expected for the nucleation of rocksalt ScN, represent the growth front of the ScN thin films. Nevertheless, the film surface is relatively smooth with a root mean square (RMS) surface roughness of 0.31 nm obtained from the AFM $2 \times 2\,\mu$m area scan (not shown).

Figure 3 shows a plan-view bright-field TEM image of the ScN film and a selected area electron diffraction (SAED) taken along the [001] zone axis. The diffraction pattern does not show any spreading of high-order diffraction spots and is consistent with a ScN film of high crystal quality. In addition, a periodic mound structure with mounds surrounded by nanopipe formations as well as dislocations is visible in the bright field image.

A high-resolution TEM image of the MgO/ScN interface is shown in Fig. 4. The insert is a corresponding SAED consisting of 002 MgO and 002 ScN overlapping reflections

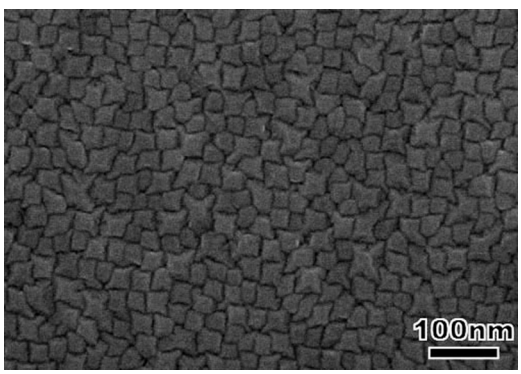

FIG. 2. Plan-view FESEM image of the ScN surface showing the formation of square flat-topped mounds with average estimated feature size of 40 nm.

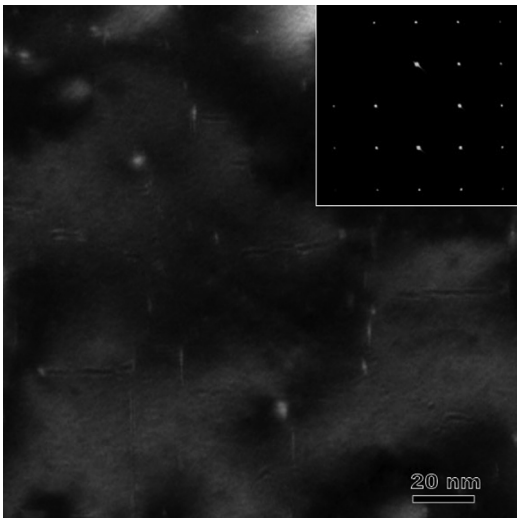

FIG. 3. Plan-view bright-field TEM image of the ScN thin film grown on MgO substrate. Insert is a SAED obtained at [001] zone axes.

that confirm the epitaxial growth of the ScN film on the MgO(001) substrate with a cube-on-cube epitaxial relationship of ScN(001)[100]||MgO(001)[100], as also obtained from XRD φ scans of 022 ScN reflections. The separation of the 002 MgO and 002 ScN reflections is consistent with a lattice mismatch of about 7% between the ScN thin film and the MgO substrate.

Hall measurements were performed at room temperature in the van der Pauw configuration. The ScN films were found to be n-type with a typical film yielding an electrical resistivity of 0.22 mΩ-cm, an electron mobility of 106 $cm^2\ V^{-1}\ s^{-1}$, and a carrier concentration of $2.5 \times 10^{20}\ cm^{-3}$. The degenerate carrier concentration can be attributed to contamination with impurities, mainly oxygen, to the presence of nitrogen vacancies, or to both. An oxygen concentration of 1.6 ± 1 at. % was obtained by RBS using NRA for improved light element detection. The fact that the mobility can be so high despite the oxygen contamination suggests that ultra-high vacuum and ultra-high purity starting material may not be required to generate ScN films with satisfactory properties for majority carrier device applications.

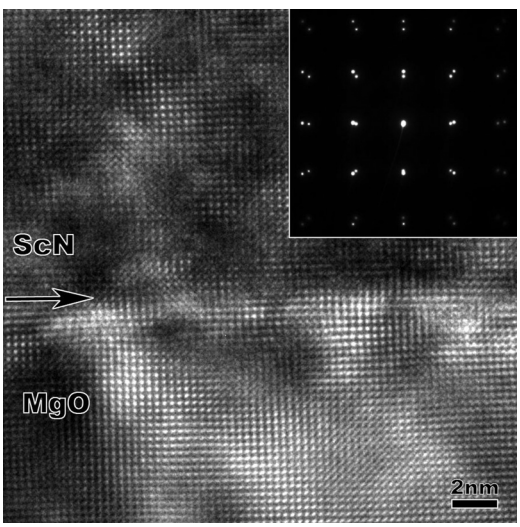

FIG. 4. High resolution TEM image of ScN/MgO interface (shown by arrow). The lattice mismatch between the ScN film and the MgO substrate is about 7%. The insert SAED confirms the epitaxial growth of ScN on MgO substrate.

Figure 5 shows (a) the in-plane electrical conductivity and (b) Seebeck coefficient for a ScN thin film as a function of temperature. The theoretically calculated values are plotted on the same graphs (blue diamonds) for comparison and will be discussed below. The conductivity shows metallic-like behavior with the value of conductivity decreasing with temperature to 1353 S/cm at 840 K. The magnitude of the Seebeck coefficient increases with temperature to a value of −156 μV/K at 840 K. To the authors' knowledge, this is the largest Seebeck coefficient reported thus far for ScN films.

In order to better understand these results and to determine whether further optimization is possible, theoretical modeling of the thermoelectric properties of ScN was performed. Given that the Seebeck coefficient (S) is relatively insensitive to scattering (and is independent of scattering in the case of a constant mean-free-path), S depends most strongly on the position of the Fermi level (E_F). For acoustic phonon scattering in parabolic energy bands, the mean-free-path is energy independent.[33] Thus, E_F is extracted by fitting the theoretical S to the experimental S. Using the fitted values of E_F, which depending on the temperature are located at 0.06-0.09 eV above the band edge (Fig. 6), the electrical conductivity is computed. By optimizing a single constant mean-free-path for backscattering, the calculated electrical

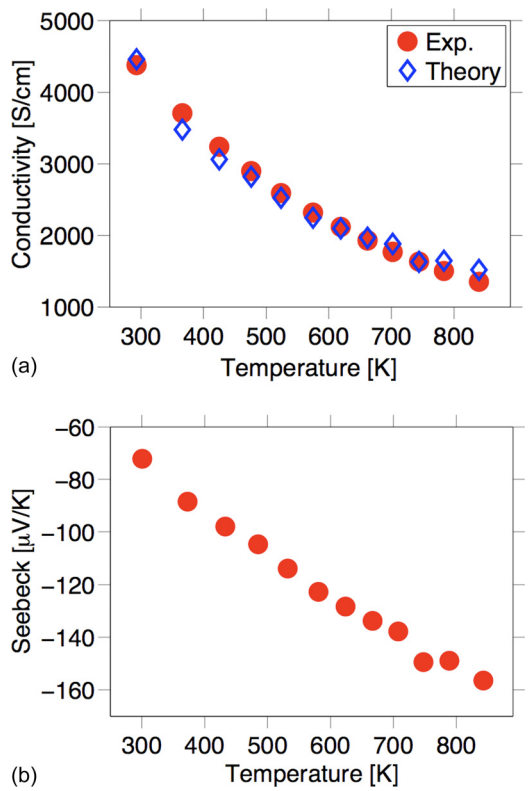

FIG. 5. (a) In-plane electrical conductivity and (b) in-plane Seebeck coefficient of a ScN film measured under vacuum in the 300-840 K temperature range. Note that the theoretical Seebeck was set equal to the experimental Seebeck in order to determine the location of the Fermi level at each temperature. The extracted Fermi level was used to compute the electrical conductivity.

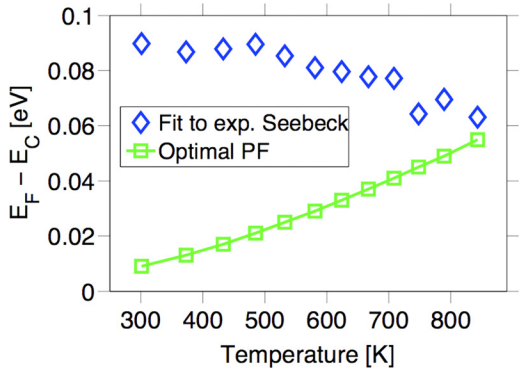

FIG. 6. Extracted Fermi level and optimal Fermi level, relative to the conduction band edge, versus temperature.

conductivity is matched to the experimental values (see Fig. 5(a)). Acoustic phonon scattering is important for obtaining the correct temperature dependence and is approximately expressed as $\lambda(T) = \lambda_0 T_0/T$, where λ_0 is the MFP at the reference temperature T_0.[33] With $\lambda_0 = 23$ nm at $T_0 = 300$ K, we obtain a good fit with experiment. Note that this MFP is similar to that of Bi_2Te_3 (18 nm) and Ge (29 nm) but is significantly smaller than that of GaAs (110 nm).[32] The extracted MFP at 300 K is roughly a half of the average mound size, thus, indicating that acoustic phonon scattering is the dominant scattering source for the experimental temperature range. The measured electrical conductivity decreases more rapidly at higher temperatures compared to theory and may be the result of additional scattering processes not considered here such as optical phonon scattering.

Figure 7 shows both experimental and theoretical power factors of ScN thin films as a function of temperature. The measured power factor increases with temperature, reaching a maximum of 3.5×10^{-3} W/mK^2 at 600 K before saturating, as can be seen from Fig. 7. This value of the power factor is comparable with that of undoped crystalline SiGe[34] and exceeds the power factor of another high temperature thermoelectric material, La_3Te_4, which has a power factor of about 0.6×10^{-3} W/mK^2 at 600 K.[35] Unlike the measured power factor, the calculated power factor does not show a

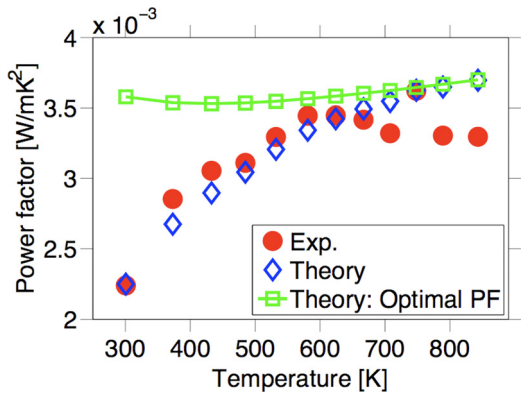

FIG. 7. Power factor of a ScN film as a function of temperature. The power factor increases with temperature reaching a maximum value of 3.5×10^{-3} W/mK^2 at 600 K. The theoretical power factor was calculated using a mean-free-path for backscattering of 23 nm at 300 K. The optimal power factor was obtained by varying the location of the Fermi level to maximize the power factor.

maximum. The discrepancy results from the slower decay of the theoretical conductivity compared to the experimental conductivity, as discussed above. Using this theoretical model, which provides a good description of the thermoelectric properties of ScN, the optimal power factor for ScN can be predicted. The optimal power factor is obtained by varying the Fermi level to achieve the largest possible value, and the result is plotted as a function of temperature in Fig. 7 (green squares). Interestingly, at high temperatures, the optimal power factor and the calculated power factor are nearly identical. Thus, at high temperature, the Fermi level is near the optimal position resulting in the large experimental power factor of ScN. At room temperature, however, the optimal power factor is significantly larger. Therefore, in principal, by adjusting E_F, the room temperature power factor can be as large as that obtained at high temperature, as can be seen in Fig. 7. According to Fig. 6, which shows the location of the Fermi level when fitting the experimental Seebeck coefficient (blue diamonds) and optimizing the power factor (green squares), having E_F near the band edge would yield the optimal power factor at 300 K.

The room temperature thermal conductivity of the same ScN film of 20.7 W/mK was measured in the cross-plane direction using TDTR technique. As expected, this value is relatively high, resulting from a significant electronic contribution to the total thermal conductivity due to the high electrical conductivity of ScN. Note that due to the film thickness and experimental set-up the thermal transport measurements could not be performed at the same direction as the measurements of the Seebeck coefficient and electrical conductivity. Temperature dependent TDTR performed on a ScN sample grown under similar conditions shows that the thermal conductivity rolls off as temperature increases reaching a value of 8.34 W/mK at 800 K.[36] Combining the in-plane power factor and cross-plane thermal conductivity would suggest a ZT value of about 0.3. Due to the measurement limitation it is common to calculate the estimated value of ZT dividing the power factor obtained in the in-plane direction by the cross-plane thermal conductivity. This approach, however, is not valid in case of anisotropic materials. Rocksalt ScN, on the other hand, is isotropic and thus, this estimated value of ZT should be close to the true value of this material. These results indicate that with optimized doping, impurity control, and suitable alloying for thermal conductivity reduction, ScN could become a promising candidate for thermoelectric power generation from waste heat as a high temperature n-type parent material.

In order to evaluate the influence of the oxygen contamination on the electronic structure and properties of the ScN the SOD technique was employed. SOD uses the space group symmetry of a particular crystal structure to obtain the symmetry inequivalent configurations (SIC) of the 222 supercell (Table I). The number of configurations calculated for a 6.25% occupancy of the anion sublattice or 3.12 at. % of total oxygen concentration decreases from 496 possible configurations to five symmetry inequivalent configurations. This significant drop in the number of distinct configurations allows investigating the entire space of configurations in order to obtain the ordering tendency of oxygen in O-doped

TABLE I. SOD technique analysis for 222 supercell with varying oxygen concentrations.

Number of different atoms	Number of configurations	Number of symmetry inequivalent configurations	O-O distance (Å)	% composition of anions
N = 30 O = 2	496	5	4.24	6.25
N = 29 O = 3	4960	14	6.05	9.37
N = 28 O = 4	35 960	71	7.34	12.50
N = 27 O = 5	201 376	223	3.00	15.62
N = 26 O = 6	906 192	874	5.20	18.75

TABLE II. Total energies of the all SIC's for a 6.25% of oxygen on nitrogen site. The lowest energy corresponds to the SIC-3 where O-O distance is the largest.

SIC	O-O distance before relaxation (Å)	Multiplicity	O-O distance after relaxation (Å)	Total energy for $Sc_{32}N_{30}O_2$ (eV)
1	4.52	48	4.52	0.150
2	6.39	48	6.39	0.004
3	7.82	16	7.82	0.000
4	3.19	192	3.16	0.078
5	5.53	192	5.53	0.003

ScN. Replacing nitrogen atoms by oxygen in the octahedrally bonded rocksalt ScN causes a slight decrease in the lattice constant of the 222 supercell from 9.04 Å to 9.00 Å for 0 and 3.12 at. % of oxygen.

In order to investigate the chemical ordering tendency of oxygen in ScN films, the total energies of the five symmetry inequivalent configurations were calculated, and the results are summarized in Table II. The calculations suggest that SIC-3, where two oxygen atoms in the 222 supercell are separated by a maximum distance of 7.82 Å, is the most energetically favored structure. The next two configurations having lower energies are SIC-2 and SIC-5, where oxygen-oxygen distances are 6.39 Å and 5.53 Å, respectively. As oxygen atoms come closer, the total energies of the structures increase (see SIC-1 and SIC-4) and the system becomes less stable. In addition, the O-O bond length in ScN does not change during the relaxation process, suggesting that oxygen tends to form solid solution alloys with nitrogen on the anion sublattice of ScN. The relative stability of SIC-3, SIC-2, and SIC-5 indicates no tendency of oxygen clustering or oxide precipitation in ScN, which otherwise could have significantly altered the electronic structure of ScN.

The electronic densities of states were calculated for 1.56, 3.12, 4.68, and 6.25 at. % oxygen-doped ScN that corresponds to 3.12%, 6.25%, 9.37%, and 12.50% of oxygen occupying the N-site, as discussed above. It has been found that the presence of oxygen in ScN does not alter the nature of the electronic states of ScN; however, the substitution of oxygen for nitrogen moves the Fermi energy from the middle of the bandgap into the conduction band as can be seen from Fig. 8. Oxygen has one extra electron and thus behaves in ScN as an n-type donor, increasing the carrier concentration. Thus, for 1.56 at. % oxygen-doped ScN, there are about 1×10^{21} oxygen atoms per cubic centimeter. If we assume that each oxygen atom donates one electron, there are $1 \times 10^{21}\,cm^{-3}$ extra electrons in the system. To accommodate this large number of extra electrons, the Fermi level moves into the conduction band. Simulations reveal that the Fermi level moves from the conduction band edge up by 0.34, 0.52, 0.73, and 0.82 eV for 1.56, 3.12, 4.68, and 6.25 at. % oxygen-doped ScN, respectively. Thus, the shift of the position of the Fermi level into the band resulted in the apparent increase of the bandgap of ScN as a function of the oxygen concentration. This is known as the Burstein-Moss shift observed in some degenerately doped semiconductors.[37] The shift of the Fermi level of about 0.5 eV was recently reported for 1.56 at. % oxygen concentration in ScN using similar simulation approach.[38] In addition, the

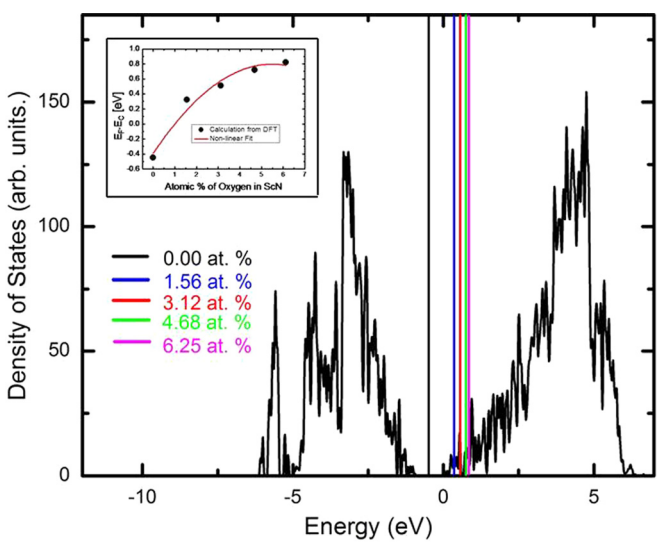

FIG. 8. Calculated densities of electronic states as a function of the oxygen content in ScN films. The Fermi energy shifts in the conduction band as the concentration of oxygen is increased in ScN from 0.00 to 6.25 at. %, while the basic electronic band structure is preserved. Insert is the second-order polynomial fit of (E_F-E_C) vs. oxygen concentration, which is used to estimate the position of the Fermi energy for oxygen content below 1.56 at. %.

incorporation of oxygen into the ScN matrix does not significantly change the shape of the DOS of pure ScN.[38]

As was discussed above, the fitting of the experimental data suggests that the Fermi level of sputtered ScN films is positioned 0.08 eV above the conduction band edge. The DFT approach predicted a 0.34 eV shift for 1.56 at. % oxygen-doped ScN. Experimentally, however, the oxygen concentration falls into an uncertainty range of 0.6-2.6 at. %. Calculations of the oxygen concentrations below 1.56 at. % were not performed due to the computational limitation of large supercells. Therefore, a second-order polynomial fit (see Fig. 8 insert) of the E_F-E_C as a function of the oxygen concentration was used to estimate the position of the Fermi level for oxygen contaminated ScN thin films at the levels below 1.56 at. %. It was found that −0.05, 0.10, 0.34, and 0.41 eV shifts of the Fermi level above the bottom of the conduction band correspond to 0.6, 1, 1.6, and 2.6 at. % oxygen, respectively. Thus, the position of the Fermi level obtained by DFT calculations and fitting of the experimental data is in a good agreement, suggesting about 1 at. % of substitutional oxygen impurities in the sputtered ScN thin films.

IV. CONCLUSIONS

The structural and thermoelectric properties of ScN(001) epitaxial thin films were studied by both experimental and theoretical techniques. We report a thermoelectric power factor of 3.3×10^{-3} W/mK^2 at 800 K for a ScN(001) thin film grown on MgO(001) by reactive magnetron sputtering. This is the highest value yet reported for ScN and is comparable with established n-type thermoelectric materials for high-temperature applications. Theoretical modeling of the thermoelectric properties of ScN is found to provide a very good fit to the experimental observations and demonstrates that the measured power factor at high temperature corresponds to the theoretical optimal value. A mean-free-path of 23 nm at 300 K and Fermi level located roughly 0.08 eV above the conduction band edge are extracted. The calculations indicate that further optimization of the power factor is possible near room temperature. First-principles DFT calculations combined with the SOD technique reveal that the presence of oxygen that contaminates the ScN thin films leads to a shift of the Fermi energy towards the conduction band without altering the overall ScN electronic structure. The oxygen doping in ScN provides the advantageous shift of the Fermi level into the conduction band resulting in improved values of the power factor at high temperature. The cross-plane thermal conductivity, however, is relatively high (~8.34 W/mK at 800 K), yielding an estimated value of $ZT = 0.3$. Further alloying and nanostructuring is needed to improve the thermoelectric properties of ScN thin films.

ACKNOWLEDGMENTS

The authors would like to thank Dr. Joseph Feser for the temperature dependent thermal conductivity measurements and Yuefeng Wang for the AFM analysis. This work was funded by DARPA/Army Research Office Contract No. W911NF0810347.

[1]K. A. Gschneider, G. A. Melson, D. A. Melson, D. H. Youngblood, and H. H. Schock, *Scandium: Its Occurrence* (Academic Press, London, 1975), Vol. 165.
[2]D. Gall, I. Petrov, L. D. Madsen, J.-E. Sundgren, and J. E. Greene, J. Vac. Sci. Technol. A **16**, 2411 (1998).
[3]D. Gall, M. Stadele, K. Jarrendahl, I. Petrov, P. Desjardins, R. T. Haasch, T.-Y. Lee, and J. E. Greene, Phys. Rev. B **63**, 125119 (2001).
[4]D. Gall, I. Petrov, N. Hellgren, L. Hultman, J. E. Sundgren, and J. E. Greene, J. Appl. Phys. **84**, 6034 (1998).
[5]A. R. Smith, H. A. H. AL-Brithen, D. C. Ingram, and D. Gall, J. Appl. Phys. **90**, 1809 (2001).
[6]J. L. Hall, M. A. Moram, A. Sanchez, S. V. Novikov, A. J. Kent, C. T. Foxon, C. J. Humphreys, and R. P. Campion, J. Cryst. Growth **311**, 2054 (2009).
[7]M. A. Moram, S. V. Novikov, A. J. Kent, C. Norenberg, C. T. Foxon, and C. J. Humphreys, J. Cryst. Growth **310**, 2746 (2008).
[8]M. A. Moram, T. B. Joyce, P. R. Chalker, Z. H. Barber, and C. J. Humphreys, Appl. Surf. Sci. **252**, 8385 (2006).
[9]D. Gall, I. Petrov, P. Desjardins, and J. E. Greene, J. Appl. Phys. **86**, 5524 (1999).
[10]M. A. Moram, Z. H. Barber, and C. J. Humphreys, Thin Solid Films **516**, 8569 (2008).
[11]J. M. Gregoire, S. D. Kirby, M. E. Turk, and R. B. van Dover, Thin Solid Films **517**, 1607 (2009).
[12]J. M. Gregoire, S. D. Kirby, G. E. Scopelianos, F. H. Lee, and R. B. van Dover, J. Appl. Phys. **104**, 074913 (2008).
[13]C. Hoglund, J. Bareno, J. Birch, B. Alling, Z. Czigany, and L. Hultman, J. Appl. Phys. **105**, 113517 (2009).
[14]S. Kerdsongpanya, N. van Nong, N. Pryds, A. Zukauskaite, J. Jensen, J. Birch, J. Lu, L. Hultman, G. Wingqvist, and P. Eklund, Appl. Phys. Lett. **99**, 232113 (2011).
[15]J. P. Dismukes, W. M. Yim, and V. S. Ban, J. Cryst. Growth **13–14**, 365 (1972).
[16]J. H. Edgar, T. Bohnen, and P. R. Hageman, J. Cryst. Growth **310**, 1075 (2008).
[17]B. Saha, J. Acharya, T. D. Sands, and U. V. Waghmare, J. Appl. Phys. **107**, 033715 (2010).
[18]A. H. A. AL-Brithen, E. M. Trifan, D. C. Ingram, A. R. Smith, and D. Gall, J. Cryst. Growth **242**, 345 (2002).
[19]M. A. Moram, M. J. Kappers, and C. J. Humphreys, Phys. Status Solidi C **7**, 1778 (2010).
[20]M. A. Moram, Y. Zhang, M. J. Kappers, Z. H. Barber, and C. J. Humphreys, Appl. Phys. Lett. **91**, 152101 (2007).
[21]M. Zebarjadi, Z. Bian, R. Singh, A. Shakouri, R. Wortman, V. Rawat, and T. Sands, J. Electron. Mater. **38**, 960 (2009).
[22]V. Rawat and T. D. Sands, J. Appl. Phys. **100**, 064901 (2006).
[23]V. Rawat, Y. K. Koh, D. G. Cahill, and T. D. Sands, J. Appl. Phys. **105**, 024909 (2009).
[24]C. A. Paddock and G. L. Eesley, J. Appl. Phys. **60**, 285 (1986).
[25]A. D. G. Cahill, Rev. Sci. Instrum. **75**, 5119 (2004).
[26]L. E. Cassels, T. E. Buehl, P. G. Burke, C. J. Palmstrom, A. C. Gossard, G. Pernot, A. Shakouri, C. R. Haughn, M. F. Doty, and J. M. O. Zide, J. Vac. Sci. Technol. B **29**, 03C114 (2011).
[27]J. P. Perdew, K. Burke, and M. Ernzerhof, Phys. Rev. Lett. **77**, 3865 (1996).
[28]D. Vanderbilt, Phys. Rev. B **41**, 7892 (1990).
[29]V. I. Anisimov and O. Gunnarson, Phys. Rev. B **43**, 7570 (1991).
[30]R. Grau-Crespo, S. Hamad, C. R. A. Catlow, and N. H. de Leeuw, J. Phys.: Condens. Matter **19**, 256201 (2007).
[31]G. D. Mahan and J. O. Sofo, Proc. Natl. Acad. Sci. U.S.A. **93**, 7436 (1996).
[32]C. Jeong, R. Kim, M. Luisier, S. Datta, and M. Lundstrom, J. Appl. Phys. **107**, 023707 (2010).
[33]M. Lundstrom, *Fundamentals of Carrier Transport* (Cambridge University Press, Cambridge, United Kingdom, 2000).
[34]H. Takiguchi, A. Matoba, K. Sasaki, Y. Okamoto, H. Miyazaki, and J. Morimoto, Mater. Trans. **51**, 878 (2010).
[35]H. L. Gao, T. J. Zhu, H. Wang, Z. F. Ren, and X. B. Zhao, J. Phys. D: Appl. Phys. **45**, 185303 (2012).
[36]P. V. Burmistrova, Ph.D. dissertation, Purdue University, West Lafayette, 2012.
[37]E. Burstein, Phys. Rev. **93**, 632 (1954).
[38]S. Kerdsongpanya, B. Alling, and P. Eklund, Phys. Rev. B **86**, 195140 (2012).